This is an open access article published under an ACS AuthorChoice License, which permits copying and redistribution of the article or any adaptations for non-commercial purposes.

ACS central science

Research Article

http://pubs.acs.org/journal/acscii

Egg-Box Structure in Cobalt Alginate: A New Approach to Multifunctional Hierarchical Mesoporous N-Doped Carbon Nanofibers for Efficient Catalysis and Energy Storage

Daohao Li,[†] Chunxiao Lv,[†] Long Liu,[†] Yanzhi Xia,[*,†] Xilin She,[†] Shaojun Guo,[*,‡] and Dongjiang Yang[*,†,§]

[†]Collaborative Innovation Centre for Marine Biomass Fibers, Materials and Textiles of Shandong Province, College of Chemical and Environmental Engineering, Qingdao University, Qingdao, P. R. China

[‡]Physical Chemistry and Applied Spectroscopy, Los Alamos National Laboratory, Los Alamos, New Mexico 87545, United States

[§]Queensland Micro- and Nanotechnology Centre (QMNC), Griffith University, Nathan, Brisbane, Queensland 4111, Australia

Supporting Information

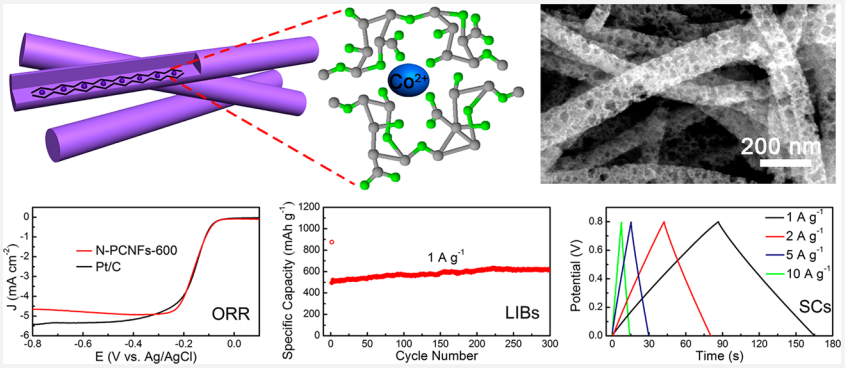

ABSTRACT: Carbon nanomaterials with both doped heteroatom and porous structure represent a new class of carbon nanostructures for boosting electrochemical application, particularly sustainable electrochemical energy conversion and storage applications. We herein demonstrate a unique large-scale sustainable biomass conversion strategy for the synthesis of earth-abundant multifunctional carbon nanomaterials with well-defined doped heteroatom level and multimodal pores through pyrolyzing electrospinning renewable natural alginate. The key part for our chemical synthesis is that we found that the egg-box structure in cobalt alginate nanofiber can offer new opportunity to create large mesopores (~10−40 nm) on the surface of nitrogen-doped carbon nanofibers. The as-prepared hierarchical carbon nanofibers with three-dimensional pathway for electron and ion transport are conceptually new as high-performance multifunctional electrochemical materials for boosting the performance of oxygen reduction reaction (ORR), lithium ion batteries (LIBs), and supercapacitors (SCs). In particular, they show amazingly the same ORR activity as commercial Pt/C catalyst and much better long-term stability and methanol tolerance for ORR than Pt/C via a four-electron pathway in alkaline electrolyte. They also exhibit a large reversible capacity of 625 mAh g^{-1} at 1 A g^{-1}, good rate capability, and excellent cycling performance for LIBs, making them among the best in all the reported carbon nanomaterials. They also represent highly efficient carbon nanomaterials for SCs with excellent capacitive behavior of 197 F g^{-1} at 1 A g^{-1} and superior stability. The present work highlights the importance of biomass-derived multifunctional mesoporous carbon nanomaterials in enhancing electrochemical catalysis and energy storage.

INTRODUCTION

As a dominant electrochemical material, carbonaceous materials have been extensively applied in energy conversion and storage applications such as proton exchange membrane fuel cells, rechargeable lithium ion batteries (LIBs), and supercapacitors (SCs) because of their low cost, outstanding cycle stability, and wide-ranging operating voltage (0−3 V).[1−5] However, the traditional carbon materials cannot satisfy the ever-increasing need for high-performance energy conversion and storage applications due to their low catalytic activity, theoretical capacity (only 372 mAh g^{-1}), and energy density (1−10 Wh kg^{-1}).[6] To improve the electrochemical performance of carbon materials without the decline of power delivery and cycle life, the most efficient strategy is to design new types of carbon nanostructures. One-dimensional (1D) carbon nanomaterials including carbon nanotubes and carbon nanofibers have been explored to replace the traditional carbon materials for energy conversion and storage applications due to their salient features (high surface area and good electrical conductivity).[7,8] In

Received: May 16, 2015
Published: August 5, 2015

 © 2015 American Chemical Society

DOI: 10.1021/acscentsci.5b00191
ACS Cent. Sci. 2015, 1, 261−269

Scheme 1. Schematic Illustration on the Synthesis Process of N-PCNFs

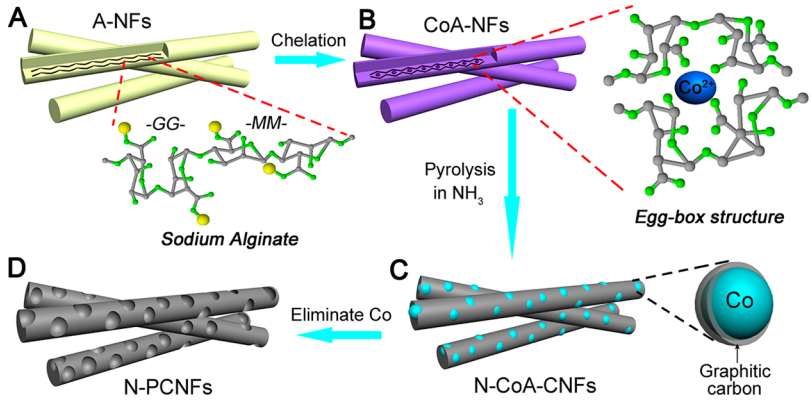

particular, chemically heteroatom (phosphorus, boron, and nitrogen) doped carbon nanotubes[9,10] and carbon nanofibers[11−13] show substantially increased electrochemical performance in comparison with heteroatom-free carbon nanomaterials.[14−16] However, the very limited mass transfer of electrolyte ions (Li^+, H^+, and OH^-) by the existing 1D carbon nanostructures makes it very hard for them to achieve very high performance in energy conversion and storage applications. In this regard, the rational design of multimodal pores on the surface of 1D carbon nanomaterials, forming 3D hierarchical structure that can offer much larger interface contact with electrolyte for promoting efficient ion diffusion to the electrode, may provide a new multifunctional platform for enhancing energy conversion and storage applications.[17,18]

Recently, biomass, as a bountiful renewable resource, is more attractive in the preparation of useful carbon materials.[19−21] With the fast development of ocean exploration, more and more attention has been paid to the utilization of abundant sea resources as the ocean occupies three-quarters of the earth's surface. Alginate, composed of β-D-mannuronate (M) and α-L-guluronate (G) monomers, is a naturally occurring nontoxic polysaccharide isolated from brown algae. Alginate has abundant carboxyl and hydroxyl groups in its polymeric carbon matrix. When all these functional groups have been converted to carbon oxides and water, the polymeric carbon matrix can be naturally converted to carbon materials upon carbonization, making alginate a suitable precursor for the fabrication of porous carbon materials.[22,23] More importantly, alginate macromolecules can be chelated with metal ions, such as Ca^{2+}, Fe^{3+}, Co^{2+}, and Ni^{2+}. The resulting complex structures have been described by the so-called "egg-box" model, in which each metal ion is coordinated to the carboxylate and hydroxyl groups of four G monomers from two adjacent chains of alginate macromolecules.[24,25] Such interesting structural characteristics of metal−alginate complexes may provide a new process for the synthesis of novel 3D carbon nanomaterials with multimodal pores because after their carbonization in an inert gas atmosphere, the obtained metal nanoparticle (NP)/C composites can be easily transformed into porous carbon nanostructures by removing the metal NPs using strong acid.

To well demonstrate such an interesting concept, herein we report a simple and effective biomass conversion strategy for a new class of ∼100 nm N-doped porous graphitic carbon nanofibers (N-PCNFs) with multimodal pores as high-performance multifunctional electrochemical materials for boosting oxygen reduction reaction (ORR), LIBs, and SCs by pyrolysis of electrospun alginate nanofibers derived from seaweed (an abundant, renewable, and nontoxic biomass). Several important features for N-PCNFs, which cannot be achieved in the previous reports, are integration of the large surface area, 3D interconnected network, multimodal pore, proper nitrogen doping, and good graphitization structure. These important characteristics not only largely enhance the conductivity of carbon materials and provide low-resistance channels for electron transport but also increase the electroactive surface area to decrease diffusion pathways and ion-transport resistance. We found that annealing treatment at 600 °C in ammonia was the optimal condition for obtaining the best N-PCNFs for energy conversion and storage applications. Significantly, N-PCNFs-600 can work as an excellent metal-free catalyst with the same electrocatalytic activity for ORR as that of Pt/C and better long-term stability and methanol tolerance for ORR than those of Pt/C via a four-electron pathway in alkaline solution. Moreover, N-PCNFs-600 as anode material exhibits a large reversible capacity of 625 mAh g^{-1} at 1 A g^{-1}, good rate capability (175 mAh g^{-1} at 20 A g^{-1}), and excellent cycling performance (625 mAh g^{-1} at 1 A g^{-1} over 300 cycles) for LIBs, which is better than N-PCNFs pyrolyzed at higher temperature and much better than N-free PCNFs. The N-PCNFs-600 also represents highly efficient carbon nanomaterials for SCs with excellent capacitive behavior of 197 F g^{-1} at 1 A g^{-1} and superior stability.

RESULTS AND DISCUSSION

Synthesis and Physical Characterization of N-PCNFs. Scheme 1 shows the typical procedure for the synthesis of the N-PCNFs. First, the electrospinning technique was used to make alginate nanofibers (A-NFs) with the alginate and PEO as spinning materials (Scheme 1A), followed by immersing them in a Co^{2+} alcohol solution to conduct the chelation of alginate macromolecule with Co^{2+}, resulting in the formation of cobalt alginate nanofibers (CoA-NFs) (Scheme 1B). In this step, the G segments of the alginate framework were aligned side-by-side to form an "egg-box" structure, in which the Co^{2+} cations were confined by their coordination with the polymer chains. As shown in Figure S1A, the broad diffraction peak at $2\theta = 21.0°$ is ascribed to a typical "egg-box" structure in G-rich Co-alginate junction zones where the 3/1 helical conformation is dominant in the low-crystallinity nanofibers.[26] The weight percentage of Co species in the CoA-NFs is determined to be about 12.96% by using thermogravimetric analysis (TGA) (Figure S1B). Then, the CoA-NFs were pyrolyzed for 1 h in NH_3 atmosphere to form Co NP decorated N-doped carbon nanofibers (N-CoA-CNFs-T) at different temperatures (T) (Scheme 1C). During

DOI: 10.1021/acscentsci.5b00191
ACS Cent. Sci. 2015, 1, 261−269

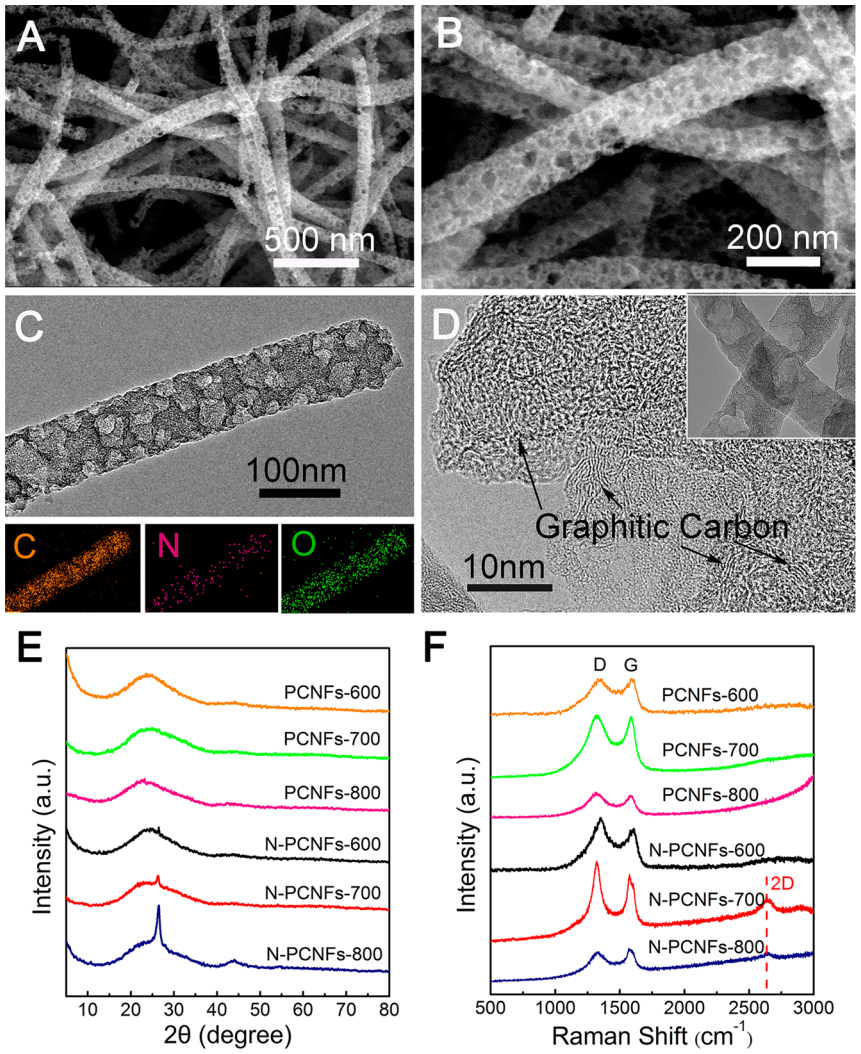

Figure 1. (A, B) SEM images of N-PCNFs-600. (C) Low-magnification TEM image and TEM-EDS mapping and (D) high-magnification TEM image of N-PCNFs-600. (E) XRD patterns and (F) Raman spectroscopy of N-PCNFs-600, PCNFs-600, PCNFs-700, PCNFs-800, N-PCNFs-700, and N-PCNFs-800.

the treatment, the Co NPs can partly catalyze the amorphous carbon into graphitic carbon in NH_3 atmosphere. Finally, the Co NPs were eliminated by acid treatment and left large-sized mesopores on the nanofibers to obtain the N-PCNFs (Scheme 1D).

The morphologies of all the samples were studied by scanning electron microscopy (SEM) and transmission electron microscopy (TEM). The A-NFs are straight and smooth with the diameter of ∼200 nm (Figure S2A). The CoA-NFs possess morphology similar to that of A-NFs (Figure S2B), meaning the chelation of alginate macromolecule with Co^{2+} does not influence the morphology of nanofibers. Figure 1A−C shows the SEM and TEM images of N-PCNFs-600. A large amount of large-sized mesopores (∼10−40 nm) are observed on the surface of CNFs, which are formed by the elimination of the Co NPs on the surface of N-Co-CNFs-600 in acid solution (Figure S2C). The diameter of N-PCNFs-600 is ∼100 nm, smaller than that of A-NFs. The size shrinkage in the carbonation process is ascribed to the release of H_2O and CO_2 during the thermal decomposition. It should be noted that other N-PCNFs-*X* (*X* = 700, 800) exhibit less abundant pores on the surface than N-PCNFs-600 (Figure S2D,E), which is caused by the aggregation of the Co NPs at high temperature. The TEM-energy dispersive X-ray elemental mappings were further used to characterize the compositions of N-PCNFs-600, showing that the C, N, and O elements are homogeneously distributed in a single nanofiber (Figure 1C). The high-resolution TEM (HRTEM) image (Figure 1D) of N-PCNFs-600 implies that it contains many semigraphitic domains. The structure of N-PCNFs-600 was further characterized using X-ray diffraction. The sharp diffraction peak located at $2\theta = 26.3°$ is characteristic of a crystalline graphitic (002) plane for N-PCNFs-600 (Figure 1E). Furthermore, N-PCNFs-800 shows another diffraction peak located at 44.3°, characteristic of the crystalline graphite (101) plane,[27,28] indicating a higher degree of graphitic carbon at higher pyrolysis temperature (Figure 1E).

The CoA-NFs were also pyrolyzed for 1 h in Ar atmosphere to get other PCNFs-*T* (*T* denotes temperature) without any nitrogen doping at different temperatures. Figure S2F−H shows the SEM images of PCNFs-600, PCNFs-700, and PCNFs-800. The large-sized mesoporous structure (∼10−40 nm) is still observed on the surface of CNFs. The difference between PCNFs-600 and N-PCNFs-600 is that the PCNFs-600 (Figures S2F and S3A) shows a bigger diameter (∼120 nm) and fewer pores than N-PCNFs-600, and also absolutely amorphous carbon rather than graphitic carbon (Figure S3B).

DOI: 10.1021/acscentsci.5b00191
ACS Cent. Sci. 2015, 1, 261−269

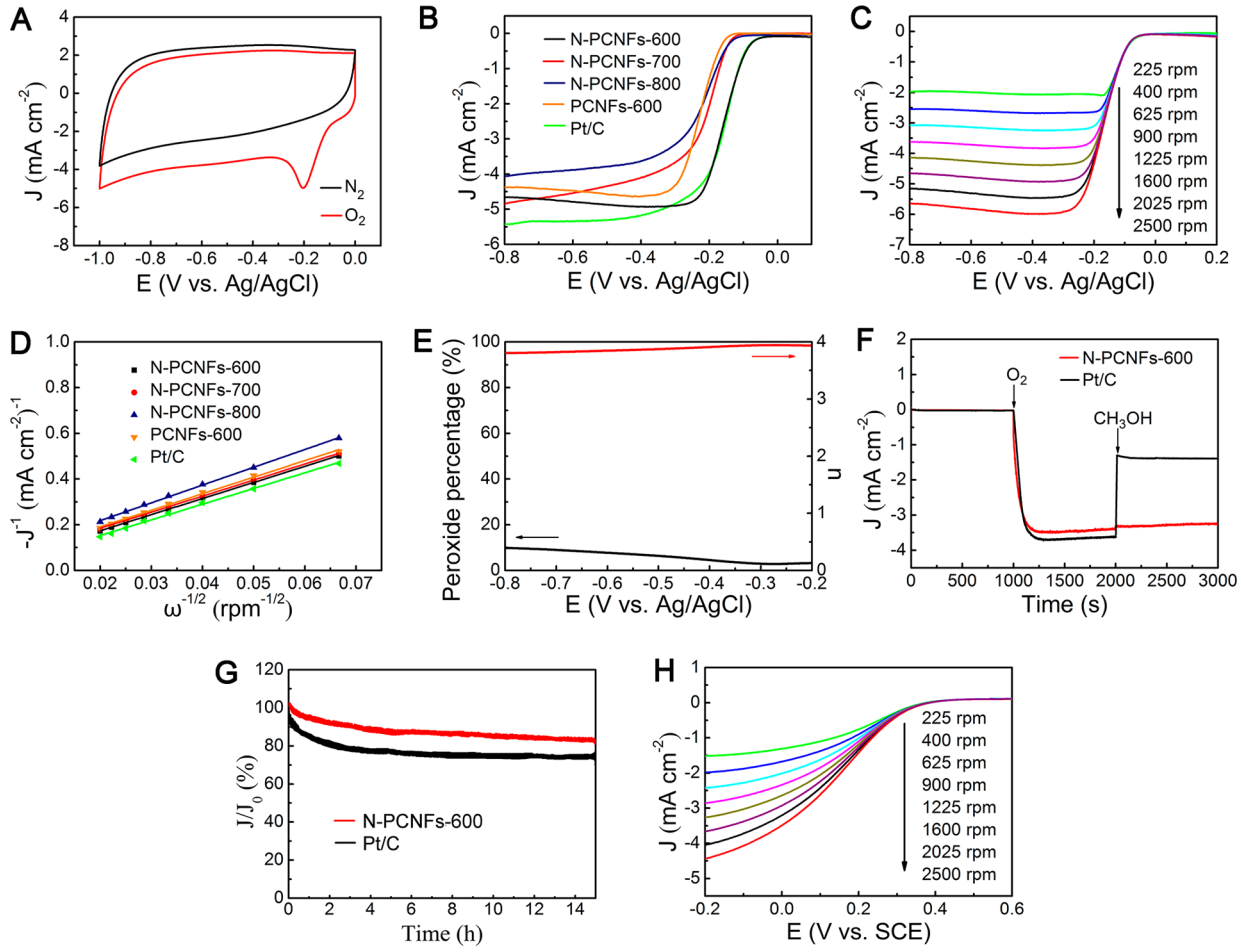

Figure 2. (A) CVs of N-PCNFs-600 in N_2- and O_2-saturated 0.1 M KOH solution. (B) RDE curves of N-PCNFs-600, N-PCNFs-700, N-PCNFs-800, PCNFs-600, and 20% Pt/C. (C) LSV curves of N-PCNFs-600 at various rotation speeds. (D) K–L plots for N-PCNFs-600, N-PCNFs-700, N-PCNFs-800, PCNFs-600, and 20% Pt/C obtained from LSVs at −0.6 V. (E) H_2O_2 yield and electron transfer number of N-PCNs-600. (F) Current–time curves of N-PCNFs-600 and 20% Pt/C at −0.27 V vs Ag/AgCl in 0.1 M KOH. (G) Long-term stability test of N-PCNFs-600 in comparison with commercial 20% Pt/C for 15 h at −0.7 V vs Ag/AgCl in O_2-saturated 0.1 M KOH. (H) LSV curves of N-PCNFs-600 at various rotation speeds in O_2-saturated 0.5 M H_2SO_4 solution.

The weaker and broader peak at 26.3° is observed in the XRD pattern of PCNFs-*T* (Figure 1E), revealing that the NH_3 atmosphere is very important for the formation of graphitic carbon in the presence of Co catalysts. This should be ascribed to the fact that the doped nitrogen atoms can decrease the interface energy between the Co catalysts and carbon nanofiber, and thus stabilize the interface and efficiently promote the formation of graphitic carbon.[29] Furthermore, the SEM images of the carbon nanofibers prepared from iron (Fe) and nickel (Ni) alginate nanofibers are displayed in Figure S4. Clearly, typical mesoporous structure can be observed on the surface of nanofibers by using Fe and Ni as sacrificial templates, indicating that our method is a general strategy to synthesize porous carbon nanofibers from alginate precursors.

Raman spectroscopy was further used to study the structure of the samples. All the Raman spectra display two prominent D-band and G-band peaks. Generally, the intensity ratio of D-band to G-band (I_D/I_G) is used to estimate the disorder degree of carbon. As shown in Figure 1F, the intensity ratios of I_D/I_G are 1.03 and 1.20 for PCNFs-600 and N-PCNFs-600, respectively, suggesting that the N-doping generates extrinsic defective structure on the carbon framework of CNFs. The defective structures in the N-PCNFs can increase active sites and thus enhance the electrochemical performance. Furthermore, the I_D/I_G of N-PCNFs-600, N-PCNFs-700, and N-PCNFs-800 are 1.20, 1.16, and 0.92, respectively, indicating the increase in the degree of graphitic crystalline structure by the catalysis of the metal at higher pyrolysis temperature.[30] The Brunauer–Emmett–Teller (BET) surface areas of N-PCNFs-600, N-PCNFs-700, and N-PCNFs-800 are 283, 355, and 713 $m^2\ g^{-1}$,[31] respectively (Figure S5A), indicating the N-PCNFs-*T* owns a higher specific BET surface area with increasing the pyrolysis temperature. The BJH pore size distribution calculated from the adsorption branch of the isotherms is shown in Figure S5B. Apparently, all the samples exhibit a typical bimodal shape of pore size distributions. The large pore centered at ∼10–40 nm is assigned to the elimination of Co NPs, and the small pore centered at ∼2.2–4.1 nm is ascribed to vacancies left by the release of H_2O and CO_2 during the thermal decomposition of the alginate.

N-PCNFs as Highly Efficient Pt-like Catalysts for ORR. The N-PCNFs-600 exhibits high electrocatalytic activity for ORR. Figure 2A shows the cyclic voltammograms (CVs) of N-PCNFs-600 in a N_2- and O_2-saturated 0.1 M KOH aqueous solution at a scan rate of 50 mV s^{-1}. No apparent peak can be found in CV obtained from the N_2-saturated solution,

DOI: 10.1021/acscentsci.5b00191
ACS Cent. Sci. 2015, 1, 261–269

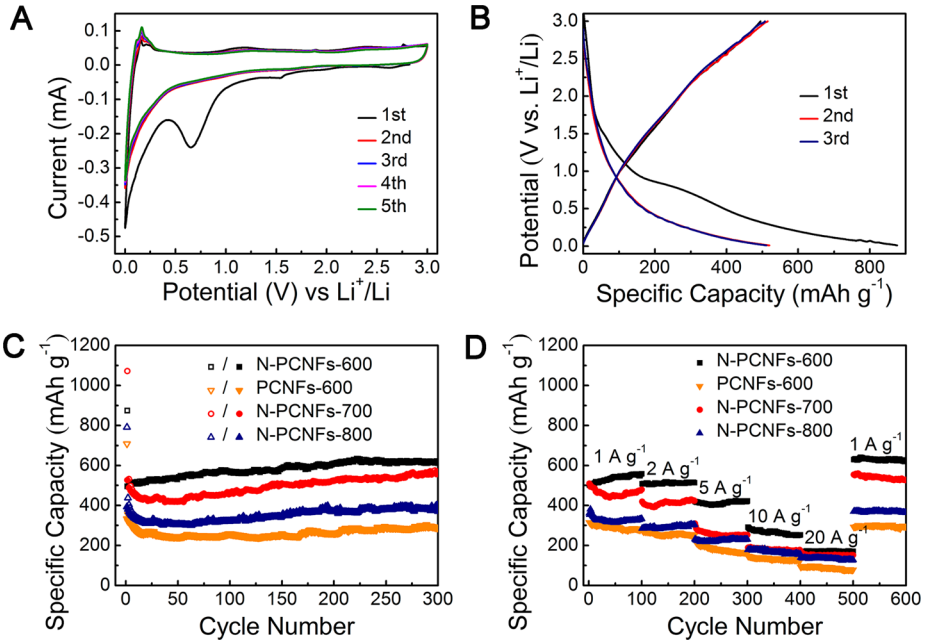

Figure 3. (A) CVs of N-PCNFs-600 at different cycles. (B) The charge and discharge curves of N-PCNFs-600 at the first, second, and third cycles between 0.01 and 3.0 V (vs Li^+/Li) at a current density of 1 A g^{-1}. (C) Specific capacity comparisons at different cycles of N-PCNFs-600, PCNFs-600, N-PCNFs-700, and N-PCNFs-800 at a current density of 1 A g^{-1}. (D) Specific capacity comparison of the N-PCNFs-600, PCNFs-600, N-PCNFs-700, and N-PCNFs-800 at different current densities.

indicating that no reaction occurs. However, a well-defined reduction peak has occurred at approximately −0.20 V (vs Ag/AgCl) in the O_2-saturated solution, indicating that O_2 is reduced on the N-PCNFs-600 catalyst. As a comparison, the CVs of N-PCNFs-700, N-PCNFs-800, and PCNFs-600 are shown in Figure S6. Apparently, their reduction peaks occur at more negative potential (<−0.20 V) than that of N-PCNFs-600. To obtain further insight into the ORR catalytic activity, the linear sweep voltammetry (LSV) measurements were performed on all samples and Pt/C (Hispec 3000 JM, 20 wt %) with a rotating disk electrode (RDE) in O_2-saturated 0.1 M KOH solution at 1600 rpm (Figure 2B). The ORR onset potential and half-wave potential of N-PCNFs-600 are −0.03 and −0.155 V, which are more positive than those of N-PCNFs-700, N-PCNFs-800, and PCNFs-600. The N-PCNFs-600 can act as a metal-free catalyst with the same half-wave potential and onset potential as those of Pt/C. LSVs were also recorded from 225 to 2500 rpm in O_2-saturated 0.1 M KOH at room temperature (Figures 2C and S7). Koutecky−Levich (K−L) plots ($-J^{-1}$ vs $\omega^{-1/2}$) were analyzed and the electron transfer number (n) was calculated on the basis of the K−L equation (Figure 2D). All plots show good linearity at different rotation speeds, and the fitting lines are near parallel over the potential range from −0.5 to −0.7 V. The n value of N-PCNFs-600 was calculated to be 3.95 at −0.6 V, indicating that the N-PCNFs-600 catalyst proceeds mainly through a four-electron mechanism. This value is better than those of the N-PCNFs-700 (3.8), N-PCNFs-800 (3.6), and PCNFs-600 (3.87). The rotating ring-disk electrode (RRDE) voltammograms of N-PCNFs-600 were also performed in O_2-saturated 0.1 M KOH electrolyte at a rotation rate of 1600 rpm to accurately determine the electron transfer number. Based on the ring and disk currents, the n value of N-PCNFs-600 was calculated to be 3.94−3.80 over the potential range from −0.2 to −0.8 V, further indicating that N-PCNFs-600 proceeds mainly by a four-electron ORR mechanism, and the H_2O_2 yield remained below 10% at all potentials (Figure 2E).

For the practical application of fuel cells, the crossover effect of small-molecule organic fuels, such as methanol, is an important consideration for cathode materials. Herein, a chronoamperometric measurement at −0.27 V with a rotating speed of 1600 rpm was performed on both N-PCNFs-600 and Pt/C electrodes to check their methanol tolerance (Figure 2F). A negative current appeared when O_2 was introduced into the N_2-saturated KOH solution at 1000 s. A significant decrease in current density is observed on Pt/C catalyst upon the addition of methanol at 2000 s. However, N-PCNFs-600 maintains stable current density after the addition of methanol. The above results indicate that the N-PCNFs-600 has better fuel selectivity toward ORR than the Pt/C. Furthermore, the durability of N-PCNFs-600 and commercial Pt/C was tested at a constant voltage of −0.7 V for 15 h in an O_2-saturated 0.1 M KOH solution at a rotation rate of 1600 rpm (Figure 2G). Remarkably, the corresponding current−time (i−t) chronoamperometric response of N-PCNFs-600 exhibits a slower decrease (16%) than that of the Pt/C (25%), indicating that the stability of N-PCNFs-600 is superior to that of the Pt/C catalyst in the alkaline medium. Furthermore, the catalytic performance of N-PCNFs-600 for ORR in O_2-saturated 0.5 M H_2SO_4 solution was examined (Figure 2H). The onset potential and half-wave potential are observed at 0.35 and 0.15 V vs a scanning calomel electrode, respectively, revealing that it has good activity for ORR in acid solution.

To rule out the effect on ORR activity from the possible retained trace Co species, X-ray photoelectron spectroscopy (XPS) measurement was carried out for N-PCNFs-600. Obviously, only the N 1s, C 1s, and O 1s peaks are observed from the XPS spectra (Figure S8). Furthermore, the catalytic performance of N-PCNFs-600 (Ca) for ORR, prepared from the calcium alginate nanofibers, was examined in O_2-saturated 0.1 M KOH solution. As shown in Figure S9A, the half-wave

DOI: 10.1021/acscentsci.5b00191
ACS Cent. Sci. 2015, 1, 261−269

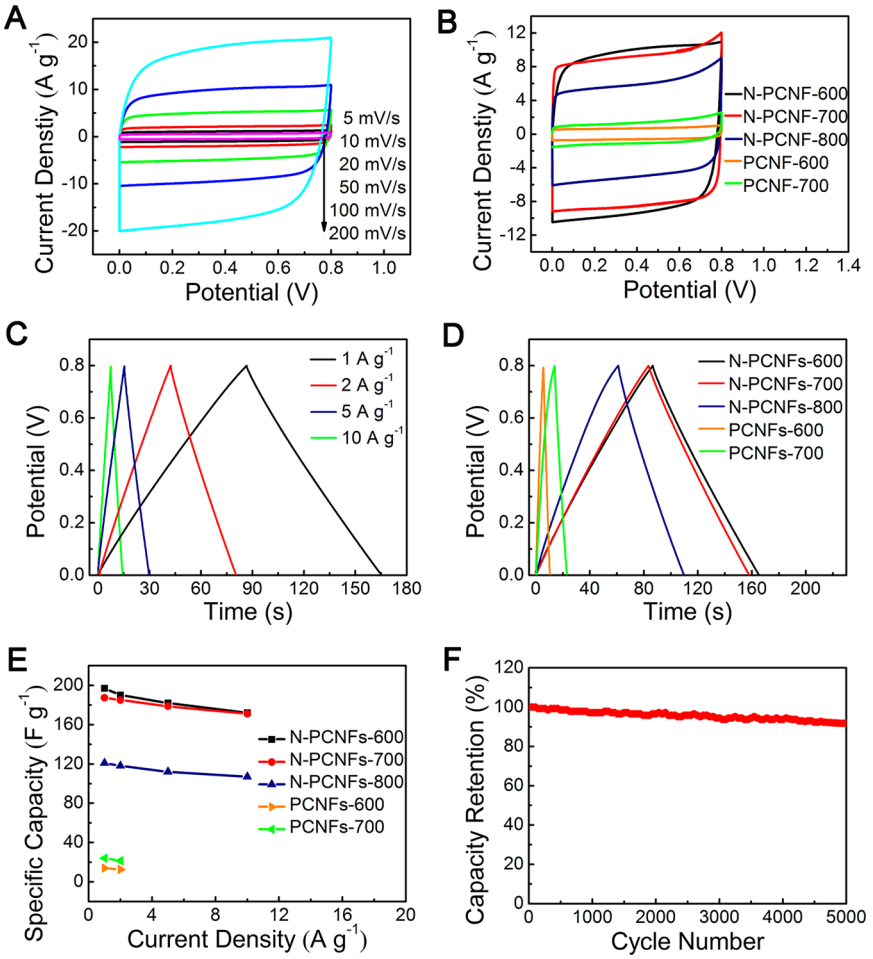

Figure 4. (A) CVs of N-PCNFs-600 SCs in 6.0 M KOH solution between 0 and 0.8 V at different scan rates. (B) CVs of different PCNF and N-PCNF in 6.0 M KOH solution at a scan rate of 100 mV s^{-1}. (C) Galvanostatic charge−discharge curves of N-PCNFs-600 at different current densities. (D) Galvanostatic charge−discharge curves of different PCNF and N-PCNF at the current density of 1 A g^{-1}. (E) The specific capacity of different PCNF and N-PCNF at various current densities. (F) Capacity retention ratio for N-PCNFs-600 at a charge−discharge current density of 5 A g^{-1} for 5000 cycles.

potential of N-PCNFs-600 (Co) for ORR is more positive than that of N-PCNFs-600 (Ca). This is probably due to the existence of Co-catalyzed more ordered graphitic carbon in N-PCNFs-600 (Co) and the disappearance of the porous structure on the surface of N-PCNFs-600 (Ca) (Figure S9B). Given that Ca is inertia for ORR, the superior ORR activity of N-PCNFs-600 should probably be ascribed to its unique structure rather than the possible remaining Co species.

N-PCNFs as High-Performance Anode Materials for LIBs. To evaluate the samples as the anode materials for LIBs, their electrochemical properties were examined by CV and galvanostatic cycling techniques. Figure 3A shows the CVs of N-PCNFs-600 in the first five cycles when the cell was set to be scanned at 0.1 mV s^{-1} in the voltage range of 0.01−3.00 V. In the first cathodic scan, the reduction peak at 0.7 V is attributed to the formation of a solid-electrolyte-interphase (SEI) film on the surface of N-PCNFs-600, which disappears from the subsequent cycles due to the dense SEI layer formed on the surface of the anode in the first discharge. Furthermore, a pair of redox peaks are observed at lower potential, in which the lithium insertion potential is quite low (close to 0 V) and the potential for lithium extraction is located in the range of 0.2−0.3 V. Peak current density and integrated area intensity are nearly unchanged in the second to fifth charge−discharge cycles, indicating that the N-PCNFs-600 offers good stability toward lithium ion insertion−extraction. The most important advantage of the N-PCNFs-600 as electrode material for LIBs is their high charge and discharge performance. Figure 3B shows the discharge−charge profiles of the N-PCNFs-600 after the first, second, and third cycles at 1 A g^{-1} in the voltage range of 0.01−3.0 V (vs Li^+/Li). During the first discharge, the voltage drops rapidly and a discharge plateau at 0.7−0.9 V is observed due to the formation of SEI, coinciding with the results from CVs. In subsequent cycles, the N-PCNFs-600 electrode shows obvious sloping charge−discharge curves and an indistinct plateau below 0.1 V. The first discharge and charge capacities of N-PCNFs-600 are 875 mAh g^{-1} and 495 mAh g^{-1} with a Coulombic efficiency of 56.6%. The initial irreversible capacity can be assigned to the formation of a SEI on the surface of electrode and the irreversible insertion of lithium ions into N-PCNFs-600. However, the capacity becomes stable and reversible after the first cycle. The N-PCNFs-600 exhibits a charge capacity of 520 and 515 mAh g^{-1} at the second and third cycles.

The performance of the N-PCNFs-600 in terms of specific capacity and cycling stability was compared with that of PCNFs-600, N-PCNFs-700, and N-PCNFs-800. As shown in Figure 3C, N-PCNFs-600 exhibits a very high reversible

DOI: 10.1021/acscentsci.5b00191
ACS Cent. Sci. 2015, 1, 261−269

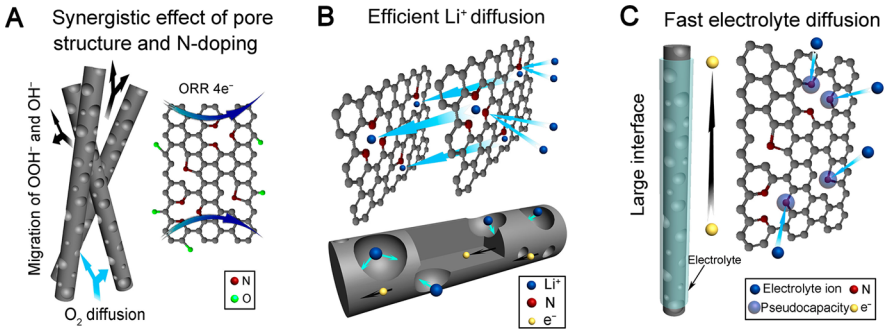

Figure 5. Schematic illustration of the advantages of N-PCNFs-600 in enhancing (A) ORR, (B) LIBs, and (C) SCs.

capacity and excellent cycling performance (625 mAh g^{-1} at 1 A g^{-1} over 300 cycles). Under identical conditions, the PCNFs-600, N-PCNFs-700, and N-PCNFs-800 present a reversible capacity of 290, 550, and 395 mAh g^{-1} after 300 cycles, respectively. To evaluate the rate performance, the samples were first charged and discharged at 1 A g^{-1} for 100 cycles, and then the current rate was stepwise increased to as high as 20 A g^{-1} for 100 cycles at each rate (Figure 3D). The N-PCNFs-600 can be reversibly charged to 516, 423, and 260 mAh g^{-1} at a current rate of 2, 5, and 10 A g^{-1} for 100 cycles, respectively. Even at a very high current rate of 20 A g^{-1}, the reversible capacity can still reach 172 mAh g^{-1} for the N-PCNFs-600, which is superior to those of the PCNFs-600 (80 mAh g^{-1}), N-PCNFs-700 (150 mAh g^{-1}), and N-PCNFs-800 (128 mAh g^{-1}). When the current density returns back to 1 A g^{-1} after 500 cycles, the reversible capacities of N-PCNFs-600, PCNFs-600, N-PCNFs-700, and N-PCNFs-800 can be increased to 632, 290, 554, and 370 mAh g^{-1}, respectively, indicating that N-PCNFs-600 shows the best performance as anode material for LIBs.

N-PCNFs as High-Performance Materials for SCs. A symmetrical two-electrode system was used to evaluate the SCs performance of the samples in 6.0 M KOH solution. Figure 4A presents the CVs of the N-PCNFs-600 for SCs at different scan rates. All of the CVs display a typical rectangular shape between 0 and 0.8 V. Other samples were also tested for comparison, showing that they also exhibit electric double layer capacitive properties (Figures 4B and S10). The galvanostatic charge−discharge curves of all samples were processed at current densities from 1 to 10 A g^{-1}. Figure 4C presents the galvanostatic charge−discharge curves of the N-PCNFs-600 with symmetric galvanostatic charge−discharge curves at all current densities. The specific capacities are determined to be 197, 190, 182, and 172 F g^{-1} at the current densities of 1, 2, 5, and 10 A g^{-1}, respectively. Furthermore, with increasing the current density up to 10 A g^{-1}, the specific capacity of N-PCNFs-600 can still keep about 87.3% of the initial value at 1 A g^{-1}, highlighting the excellent rate capability of N-PCNFs-600. As shown in the comparative galvanostatic charge−discharge curves of all the samples at current density of 1 A g^{-1} (Figures 4D and S11), the discharging time of the N-PCNFs-600 is longer compared with those of other samples, indicating that the N-CNFs-600 offers a higher capacity, being in accordance with CV results. Moreover, the galvanostatic charge−discharge curves of N-CNFs-600 and N-PCNFs-700 show higher symmetry than those of other samples.

The specific capacities at different current densities are shown in Figure 4E. It is found that the N-PCNFs-600 has the highest specific capacity of 197 F g^{-1} at 1 A g^{-1}, which is 14 times higher than that of N-free PCNFs-600. Also, compared with N-PCNFs-700 and N-PCNFs-800, the N-PCNFs-600 with the highest content of doped nitrogen (Table S1) exhibits the highest specific capacity. A long cycle life is an important concern for practical applications of SCs. To investigate the stability of the N-PCNFs-600, the galvanostatic charge−discharge cycling tests were performed at a current density of 5 A g^{-1} for 5000 cycles. As shown in Figure 4F, N-PCNFs-600 can have 91.7% initial specific capacity after 5000 cycles, indicating its good cycling stability for SCs.

Discussion. As a metal-free ORR catalyst, the unique structure of N-PCNFs-600 is favorable for boosting ORR in an alkaline solution. The numerous mesopores (∼2−40 nm) and defects on N-PCNFs-600 by the N-doping process make proton efficiently transferred. For instance, its unique large pores (∼10−40 nm) on the surface of nanofibers can facilitate the O_2 diffusion and the migration of superoxide and hydroxyl, which are rate-determining for the whole reaction (Figure 5A), and the small mesopores on the surface of the nanofibers (∼4 nm) are favorable for the adsorption of O_2 molecules.[32,33] The pyridinic- and pyrrolic-type N (revealed by XPS, Figure S8B) existing on N-PCNFs-600 can exert the electron release on carbon framework to enhance the ORR activity.[34,35]

The unique N-doped porous structure of N-PCNFs-600 also contributes to its high capacity, excellent rate ability, and long-term cycle stability for LIBs. As illustrated in Figure 5B, the 1D morphology and the part of graphitization structure of the CNFs can serve as the channels for fast electron transport, which is crucial for promoting electrochemical performance.[36−38] A large number of large-sized mesopores left by eliminating metal and small-sized mesopores by the pyrolysis process in N-PCNFs can store the electrolyte as the "reservoirs", thus shortening the diffusion distance of Li^+, and increasing the interface between active materials and electrolyte to absorb the Li^+ and also promoting rapid charge-transfer reaction.[32] The N-doping process generates extrinsic defects in the carbon frameworks to allow more Li^+ to diffuse from the outside to inside, thus allowing for the use of unexplored carbon.[15,39] Furthermore, the N-doped graphitic carbon can improve the electrochemical reactivity and conductivity to enable fast electron transport (proved by the impedance spectroscopy of Figure S12).[40] The nitrogen atoms own a lone pair of electrons, and the electronegativity of nitrogen is higher than that of carbon, which can break the electroneutrality of carbon to create the active sites. Additionally, the N-doping sites are more favorable to bind with Li^+, resulting in increased electrochemical performance. These important characteristics make N-PCNFs-600 with the highest content of nitrogen atom show the highest reversible capacity (Table S1).

DOI: 10.1021/acscentsci.5b00191
ACS Cent. Sci. 2015, 1, 261−269

As the electrode material for SCs, the specific capacity of N-PCNFs-600 is the highest among all the N-doped and N-free PCNFs. As is known, the performance of SCs depends on adsorption−desorption between active material and electrolyte (electric double layer capacitors), or the redox reaction of electrode materials (pseudocapacitors). The porous structure of N-PCNFs can increase the interface between active materials and electrolyte for enhancing the double layer capacity.[33] The mesoporous structure can provide short ion-transport and low inner-pore resistance pathways for the ions through the porous structure.[41] The N-doping process can enhance the electrical conductivity of PCNFs.[42−44] Also the pyridinic- and pyrrolic-type N existing on N-PCNFs-600 can act as the electron donor or enhance the charge density of the space charge layer for promoting the chemisorption of the electrolyte ions and therefore generating pseudocapacity (Figure 5C).[45−47] Therefore, the doped nitrogen atoms play an important role in improving the performance of SCs.

CONCLUSION

To summarize, we demonstrate the first example of the use of sustainable earth-abundant biomass as new precursors for the controlled synthesis of high-performance multifunctional nanostructured carbon energy materials with multimodal pores for efficient energy storage and catalysis. The egg-box structure in the cobalt alginate nanofiber has been used to create large mesopores (∼10−40 nm) on the surface of nitrogen-doped carbon nanofibers. The N-PCNFs-600 can act as an excellent metal-free catalyst with ORR activity identical with that of Pt and much higher stability and higher methanol tolerance for ORR via a four-electron pathway in alkaline medium than the commercial Pt/C. Significantly; it also exhibits a high specific capacity, excellent cycling performance, and good rate capability for LIBs and SCs. Given the renewability of the seaweed resource, the present work opens a new way in the use of earth-abundant materials for developing future high-performance multifunctional energy carbon nanomaterials for energy storage and catalysis on a large scale via a really "green" pathway.

METHODS

Details on materials and methods are available in the Supporting Information.

ASSOCIATED CONTENT

Supporting Information

The following file is available free of charge on the ACS Publications website at DOI: 10.1021/acscentsci.5b00191.

Experimental materials and methods, more information on morphology and structure analysis, and electrochemical data in Figures S1−S12 and Table S1 (PDF)

AUTHOR INFORMATION

Corresponding Authors

*E-mail: d.yang@griffith.edu.au
*E-mail: xiayzh@qdu.edu.cn
*E-mail: sguo@lanl.gov or shaojun.guo.nano@gmail.com.

Notes

The authors declare no competing financial interest.

ACKNOWLEDGMENTS

This work was financially supported by the National Natural Science Foundation of China (50673046), the High-Tech Research and Development Program of China (863 Program) (2010AA093701), and ARC Discovery Project (No. 130104759).

REFERENCES

(1) Zhai, Y.; Dou, Y.; Zhao, D.; Fulvio, D. F.; Mayes, R. T.; Dai, S. Carbon Materials for Chemical Capacitive Energy Storage. *Adv. Mater.* **2011**, *23*, 4828−4850.
(2) Beguin, F.; Presser, V.; Balducci, A.; Frackowiak, E. Carbons and electrolytes for advanced supercapacitors. *Adv. Mater.* **2014**, *26*, 2219−2251.
(3) Ye, T. N.; Lv, L. B.; Li, X. H.; Xu, M.; Chen, J. S. Strongly veined carbon nanoleaves as a highly efficient metal-free electrocatalyst. *Angew. Chem., Int. Ed.* **2014**, *53*, 6905−6909.
(4) Tarascon, J.-M.; Armand, M. Issues and challenges facing rechargeable lithium batteries. *Nature* **2001**, *414*, 359−367.
(5) Wang, G.; Zhang, L.; Zhang, J. A review of electrode materials for electrochemical supercapacitors. *Chem. Soc. Rev.* **2012**, *41*, 797−828.
(6) Wu, Y. P.; Rahm, E.; Holze, R. Carbon anode materials for lithium ion batteries. *J. Power Sources* **2003**, *114*, 228−236.
(7) Niu, Z.; Zhou, W.; Chen, J.; Feng, G.; Li, H.; Ma, W.; Li, J.; Dong, H.; Ren, Y.; Zhao, D.; Xie, S. Compact-designed supercapacitors using free-standing single-walled carbon nanotube films. *Energy Environ. Sci.* **2011**, *4*, 1440−1446.
(8) Chung, H. T.; Won, J. H.; Zelenay, P. Active and stable carbon nanotube/nanoparticle composite electrocatalyst for oxygen reduction. *Nat. Commun.* **2013**, *4*, 1922.
(9) Shin, W. H.; Jeong, H. M.; Kim, B. G.; Kang, J. K.; Choi, J. W. Nitrogen-doped multiwall carbon nanotubes for lithium storage with extremely high capacity. *Nano Lett.* **2012**, *12*, 2283−2288.
(10) Chen, P.; Xiao, T.-Y.; Qian, Y.-H.; Li, S.-S.; Yu, S.-H. A nitrogen-doped graphene/carbon nanotube nanocomposite with synergistically enhanced electrochemical activity. *Adv. Mater.* **2013**, *25*, 3192−3196.
(11) Chen, Y.; Li, X.; Park, K.; Song, J.; Hong, J.; Zhou, L.; Mai, Y. W.; Huang, H.; Goodenough, J. B. Hollow carbon-nanotube/carbon-nanofiber hybrid anodes for Li-ion batteries. *J. Am. Chem. Soc.* **2013**, *135*, 16280−16283.
(12) Chen, Y.; Li, X.; Zhou, X.; Yao, H.; Huang, H.; Mai, Y. W.; Zhou, L. Hollow-tunneled graphitic carbon nanofibers through Ni-diffusion-induced graphitization as high-performance anode materials. *Energy Environ. Sci.* **2014**, *7*, 2689−2696.
(13) Chen, L.; Huang, Z.; Liang, H.; Yao, W.; Yu, Z.; Yu, S. Flexible all-solid-state high-power supercapacitor fabricated with nitrogen-doped carbon nanofiber electrode material derived from bacterial cellulose. *Energy Environ. Sci.* **2013**, *6*, 3331−3338.
(14) Paraknowitsch, J. P.; Thomas, A. Doping carbons beyond nitrogen: an overview of advanced heteroatom doped carbons with boron, sulphur and phosphorus for energy applications. *Energy Environ. Sci.* **2013**, *6*, 2839−2855.
(15) Wood, K. N.; O'Hayre, R.; Pylypenko, S. Recent progress on nitrogen/carbon structures designed for use in energy and sustainability applications. *Energy Environ. Sci.* **2014**, *7*, 1212−1249.
(16) Zhang, Y.; Zhang, J.; Su, D. S. Substitutional doping of carbon nanotubes with heteroatoms and their chemical applications. *ChemSusChem* **2014**, *7*, 1240−1250.
(17) Ji, L.; Lin, Z.; Alcoutlabi, M.; Zhang, X. Recent developments in nanostructured anode materials for rechargeable lithium-ion batteries. *Energy Environ. Sci.* **2011**, *4*, 2682−2699.
(18) Dai, L.; Chang, D. W.; Baek, J. B.; Lu, W. Carbon nanomaterials for advanced energy conversion and storage. *Small* **2012**, *8*, 1130−1166.
(19) Chen, L.-F.; Huang, Z.-H.; Liang, H.-W.; Gao, H.-L.; Yu, S.-H. Three-dimensional heteroatom-doped carbon nanofiber networks

DOI: 10.1021/acscentsci.5b00191
ACS Cent. Sci. 2015, 1, 261−269

derived from bacterial cellulose for supercapacitors. *Adv. Funct. Mater.* **2014**, *24*, 5104−5111.
(20) Tenhaeff, W. E.; Rios, O.; More, K.; McGuire, M. A. Highly robust lithium ion battery anodes from lignin: an abundant, renewable, and low-cost material. *Adv. Funct. Mater.* **2014**, *24*, 86−94.
(21) Wang, S. X.; Yang, L.; Stubbs, L. P.; Li, X.; He, C. Lignin-derived fused electrospun carbon fibrous mats as high performance anode materials for lithium ion batteries. *ACS Appl. Mater. Interfaces* **2013**, *5*, 12275−12282.
(22) Wu, X. L.; Chen, L. L.; Xin, S.; Yin, Y. X.; Guo, Y. G.; Kong, Q. S.; Xia, Y. Z. Preparation and li storage properties of hierarchical porous carbon fibers derived from alginic acid. *ChemSusChem* **2010**, *3*, 703−707.
(23) Li, D.; Yang, D.; Zhu, X.; Jing, D.; Xia, Y.; Ji, Q.; Cai, R.; Li, H.; Che, Y. Simple pyrolysis of cobalt alginate fibres into Co_3O_4/C nano/microstructures for a high-performance lithium ion battery anode. *J. Mater. Chem. A* **2014**, *2*, 18761−18766.
(24) Fourest, E.; Volesky, B. Alginate properties and heavy metal biosorption by Marine Algae. *Appl. Biochem. Biotechnol.* **1997**, *67*, 215−226.
(25) Braccini, I.; Perez, S. Molecular basis of Ca^{2+} induced gelation in alginates and pectins: The egg-box model revisited. *Biomacromolecules* **2001**, *2*, 1089−1096.
(26) Li, L.; Fang, Y.; Vreeker, R.; Appelqvist, I.; Mendes, E. Reexamining the Egg-Box Model in Calcium-Alginate Gels with X-ray Diffraction. *Biomacromolecules* **2007**, *8*, 464−468.
(27) Lei, Z.; Xiao, Y.; Dang, L.; You, W.; Hu, G.; Zhang, J. Nickel-Catalyzed Fabrication of SiO_2, TiO_2/graphitized carbon, and the resultant graphitized carbon with periodically macroporous structure. *Chem. Mater.* **2007**, *19*, 477−484.
(28) Yoon, S. B.; Chai, G. S.; Kang, K.; Yu, J.-S.; Gierszal, K. P.; Jaroniec, M. Graphitized pitch-based carbons with ordered nanopores synthesized by using colloidal crystals as templates. *J. Am. Chem. Soc.* **2005**, *127*, 4188−4189.
(29) Pattinson, S. W.; Diaz, R. E.; Stelmashenko, N. A.; Windle, A. H.; Ducati, C.; Stach, E. A.; Koziol, K. K. K. In situ observation of the effect of nitrogen on carbon nanotube synthesis. *Chem. Mater.* **2013**, *25*, 2921−2923.
(30) Weingarth, D. M.; Zeiger, M.; Jäckel, N.; Aslan, M.; Feng, G.; Presser, V. Graphitization as a universal tool to tailor the potential-dependent capacitance of carbon supercapacitors. *Adv. Energy Mater.* **2014**, *4*, 1400316.
(31) Kruk, M.; Jaroniec, M. Gas adsorption characterization of ordered organic-inorganic nanocomposite materials. *Chem. Mater.* **2001**, *13*, 3169−3183.
(32) Li, Y.; Fu, Z.-Y.; Su, B.-L. Hierarchically structured porous materials for energy conversion and storage. *Adv. Funct. Mater.* **2012**, *22*, 4634−4667.
(33) Dutta, S.; Bhaumik, A.; Wu, K. C.-W. Hierarchically porous carbon derived from polymers and biomass: effect of interconnected pores on energy applications. *Energy Environ. Sci.* **2014**, *7*, 3574−3592.
(34) Nam, G.; Park, J.; Kim, S. T.; Shin, D. B.; Park, N.; Kim, Y.; Lee, J. S.; Cho, J. Metal-free Ketjenblack incorporated nitrogen-doped carbon sheets derived from gelatin as oxygen reduction catalysts. *Nano Lett.* **2014**, *14*, 1870−1876.
(35) Wei, W.; Liang, H.; Parvez, K.; Zhuang, X.; Feng, X.; Mullen, K. Nitrogen-doped carbon nanosheets with size-defined mesopores as highly efficient metal-free catalyst for the oxygen reduction reaction. *Angew. Chem., Int. Ed.* **2014**, *53*, 1570−1574.
(36) Yan, M.; Wang, F.; Han, C.; Ma, X.; Xu, X.; An, Q.; Xu, L.; Niu, C.; Zhao, Y.; Tian, X.; Hu, P.; Wu, H.; Mai, L. Nanowire Templated Semihollow Bicontinuous Graphene Scrolls: Designed Construction, Mechanism, and Enhanced Energy Storage Performance. *J. Am. Chem. Soc.* **2013**, *135*, 18176−18182.
(37) Mai, L.; Tian, X.; Xu, X.; Chang, L.; Xu, L. Nanowire Electrodes for Electrochemical Energy Storage Devices. *Chem. Rev.* **2014**, *114*, 11828−11862.
(38) Zhang, H.; Sun, X.; Huang, X.; Zhou, L. Encapsulation of alpha-Fe_2O_3 Nanoparticles in Graphitic Carbon Microspheres as High-Performance Anode Materials for Lithium-Ion Batteries. *Nanoscale* **2015**, *7*, 3270−3275.
(39) Xie, J. L.; Guo, C. X.; Li, C. M. Construction of One-dimensional Nanostructures on Graphene for Efficient Energy Conversion and Storage. *Energy Environ. Sci.* **2014**, *7*, 2559−2579.
(40) Wu, Z.-S.; Ren, W.; Xu, L.; Li, F.; Cheng, H.-M. Doped Graphene Sheets as Anode Materials with Superhigh Rate and Large Capacity for Lithium Ion Batteries. *ACS Nano* **2011**, *5*, 5463−5471.
(41) Wang, D.-W.; Li, F.; Liu, M.; Lu, G. Q.; Cheng, H.-M. 3D Aperiodic Hierarchical Porous Graphitic Carbon Material for High-Rate Electrochemical Capacitive Energy Storage. *Angew. Chem.* **2008**, *120*, 379−382.
(42) Chen, L.-F.; Zhang, X.-D.; Liang, H.-W.; Kong, M.; Guan, Q.-F.; Chen, P.; Wu, Z.-Y.; Yu, S.-H. Synthesis of Nitrogen-Doped Porous Carbon Nanofibers as an Efficient Electrode Material for Supercapacitors. *ACS Nano* **2012**, *6*, 7092−7102.
(43) Wei, J.; Zhou, D.; Sun, Z.; Deng, Y.; Xia, Y.; Zhao, D. A Controllable Synthesis of Rich Nitrogen-Doped Ordered Mesoporous Carbon for CO_2 Capture and Supercapacitors. *Adv. Funct. Mater.* **2013**, *23*, 2322−2328.
(44) Wen, Z.; Wang, X.; Mao, S.; Bo, Z.; Kim, H.; Cui, S.; Lu, G.; Feng, X.; Chen, J. Crumpled Nitrogen-Doped Graphene Nanosheets with Ultrahigh Pore Volume for High-Performance Supercapacitor. *Adv. Mater.* **2012**, *24*, 5610−5616.
(45) Fang, Y.; Luo, B.; Jia, Y.; Li, X.; Wang, B.; Song, Q.; Kang, F.; Zhi, L. Renewing Functionalized Graphene as Electrodes for High-Performance Supercapacitors. *Adv. Mater.* **2012**, *24*, 6348−6355.
(46) Seredych, M.; Hulicova-Jurcakova, D.; Lu, G. Q.; Bandosz, T. J. Surface Functional Groups of Carbons and the Effects of their Chemical Character, Density and Accessibility to Ions on Electrochemical Performance. *Carbon* **2008**, *46*, 1475−1488.
(47) Wang, D.-W.; Li, F.; Chen, Z.-G.; Lu, G. Q.; Cheng, H.-M. Synthesis and Electrochemical Property of Boron-Doped Mesoporous Carbon in Supercapacitor. *Chem. Mater.* **2008**, *20*, 7195−7200.

DOI: 10.1021/acscentsci.5b00191
ACS Cent. Sci. 2015, 1, 261−269